



## Extrusion dynamics of deep-water volcanoes

Qiliang Sun<sup>1,2,3</sup>, Christopher A-L. Jackson<sup>4</sup>, Craig Magee<sup>4,5</sup>, Samuel J. Mitchell<sup>6</sup> and Xinong Xie<sup>1,3</sup>

<sup>1</sup>Key Laboratory of Tectonics and Petroleum Resources, China University of Geosciences (Wuhan),  
Ministry of Education, Wuhan 430074, China;

<sup>2</sup>Laboratory for Marine Mineral Resources, Qingdao National Laboratory for Marine Science and  
Technology, Qingdao 266061, China;

<sup>3</sup>College of Marine Science and Technology, China University of Geosciences (Wuhan), Wuhan,  
Hubei 430074, PR China;

<sup>4</sup>Basins Research Group (BRG), Department of Earth Science & Engineering, Imperial College,  
London, SW7 2BP, UK

<sup>5</sup>School of Earth and Environment, University of Leeds, Leeds, LS2 9JT, UK

<sup>6</sup>School of Earth Sciences, University of Bristol, Bristol, BS8 1RJ UK

### Abstract

Submarine volcanism accounts for c. 75% of the Earth's volcanic activity. Yet difficulties with  
imaging their exteriors and interiors mean the **extrusion dynamics** and erupted volumes of deep-  
water volcanoes remain poorly understood. Here, we use high-resolution 3-D seismic reflection data  
to examine the external and internal geometry, ~~and extrusion dynamics~~ of two Late Miocene-  
Quaternary, deep-water (>2 km emplacement depth) volcanoes buried beneath 55–330 m of  
sedimentary strata in the South China Sea. The volcanoes have crater-like basal contacts, which  
truncate underlying strata, and erupted lava flows that feed lobate lava fans. The lava flows are >9





23 km long and contain **lava tubes** that have rugged basal contacts defined by  $\sim 90 \pm 23$  m high erosional  
24 ramps. We suggest the lava flows eroded down into and were emplaced ~~at shallow sub-surface~~  
25 ~~depths~~ within wet, unconsolidated, near-seafloor sediments. **Extrusion dynamics** were likely  
26 controlled by low magma viscosities, high hydrostatic pressures, and soft, near-seabed sediments,  
27 which collectively are characteristic of deep-water environments. ~~Because the lava flows and~~  
28 ~~volcanic edifices are imaged in 3D,~~ we calculate the lava flows account for 50–97% of the total  
29 erupted volume. ~~Our results indicate deep-water~~ volcanic edifices ~~may~~ thus form a minor  
30 component ( $\sim 3$ –50%) of the extrusive ~~system, and that~~ accurate estimates of erupted volume  
31 requires knowledge of the basal surface ~~of genetically related lava flows~~. We conclude that 3D  
32 seismic reflection data is a powerful tool for constraining the geometry and ~~extrusion dynamics~~ of  
33 buried, deep-water volcanic features; such data ~~should~~ be used to image and quantify **extrusion**  
34 **dynamics** of modern deep-water volcanoes.

35

## 36 Keywords

37 Volcano, deep-water, lava flow, seismic reflection, South China Sea

38

## 39 1. Introduction

40 The external morphology of volcanoes and their eruptive products reflect, and provide insights  
41 into, the processes controlling magma extrusion and volcano construction (e.g. Walker, 1993;  
42 Planke et al., 2000; Grosse and Kervyn, 2018). By ~~extracting~~ high-resolution, quantitative data on  
43 the morphology of modern ~~and, in some cases, still active~~ volcanic edifices and surrounding lava  
44 flows from airborne/shuttle radar topography or time-lapse multi-beam bathymetry, we can estimate



erupted volume and reconstruct volcano growth mechanisms (e.g. Holcomb et al., 1988; Walker, 1993; Goto and McPhie, 2004; Cocchi et al., 2016; Somoza et al., 2017; Allen et al., 2018; Grosse and Kervyn, 2018). Whilst remote sensing data capture the external morphology of volcanoes and lava flows, they do not image their basal surface or internal architecture. Without access to the full 3D structure of these extrusive systems, it is difficult to assess the accuracy of estimated volumes of erupted material, or test volcano growth and lava emplacement models.

Several studies demonstrate that seismic reflection data can be used to map the external morphology and internal architecture of buried volcanoes in 3D (e.g. Planke et al., 2000; Calvès et al., 2011; Jackson, 2012; Magee et al., 2013; Reynolds et al., 2017). To-date, most seismic-based studies have focused on volcanoes formed in sub-aerial or shallow-marine environments (e.g. Planke et al., 2000; Jackson, 2012; Magee et al., 2013; Reynolds et al., 2018), although seismic reflection surveys have been used to image the shallowly buried flanks of deep-water volcanoes (e.g. Funck et al. 1996). The 3D geometry, internal structure, extrusion dynamics, and volume of deep-water volcanoes thus remain poorly documented.

We use high-resolution 3D seismic reflection data to examine the external morphology and internal architecture of two, Late Miocene-Quaternary submarine volcanoes that were emplaced in deep-water (>2.0 km) on highly stretched continental crust in the northern South China Sea (Fig. 1). The volcanoes and associated lava flows are now buried by a ~55–330 m thick sedimentary succession (Fig. 1). By interpreting volcano and lava flow 3D structure, distribution, and size, we aim to determine extrusion dynamics, calculate accurate erupted volumes, and relate our findings to deep-water volcanoes studied using bathymetry and remote sensing data. We show basal surfaces of volcanic edifices and lava flows are rugged, with 50–97% of the total erupted material hosted



67 within the latter; i.e. the volcano edifices only comprise ~~only~~ a small portion of the total erupted  
68 ~~magma~~ volume. We suggest the high hydrostatic pressure of the deep-water environment controlled  
69 erupting lava rheology and, consequently, volcano and lava flow morphology and run-out distance.  
70 Our results also show erupted volumes calculated from airborne/shuttle radar topography or time-  
71 lapse multi-beam bathymetry data, which typically assume imaged volcanoes and lava flows have  
72 a smooth base, may be grossly underestimated.



73

## 74 2. Geological setting

75 The study area is located ~~in the~~ south of Pearl River Mouth Basin, on the northern, highly  
76 stretched continental crust of the South China Sea (Franke, 2013; Zhao et al., 2016) (Fig. 1a). The  
77 South China Sea was an area of subduction in the late Mesozoic, before the onset of continental  
78 rifting and subsequent seafloor spreading (~33-15 Myr) in the Cenozoic (e.g. Taylor and Hayes,  
79 1983; Briaies et al., 1993; Franke et al., 2014; Li et al., 2014; Sun et al., 2014a; Ding and Li, 2016).  
80 A lack of seaward-dipping reflections (SDRs); and low volumes of rift-related igneous rocks;  
81 suggest the northern part of the South China Sea is a magma-poor margin (e.g. Clift et al., 2001;  
82 Yan et al., 2006; Cameselle et al., 2017). Seafloor spreading ceased at ~15 Ma (Li et al., 2014), with  
83 post-rift thermal cooling driving subsidence of the northern South China Sea margin since the Early  
84 Miocene (Ru and Pigott, 1986; Yu, 1994). During this phase of thermal subsidence the Dongsha  
85 Event (~5.3 Ma) occurred, which involved widespread uplift and normal faulting (e.g. Lüdmann et  
86 al., 2001). Several mechanisms may have triggered the Dongsha Event, including the collision  
87 between Taiwan and the East Asian continent (Lüdmann et al., 2001; Hall, 2002), isostatic rebound  
88 (Zhao et al., 2012), post-rift magmatism (Franke, 2013), lithospheric bending (Wu et al., 2014),



89 and/or subduction of the South China Sea beneath the Philippine Sea plate (Xie et al., 2017).

90 Post-spreading magmatism in the South China Sea may reflect ascent of magma triggered by

91 subduction of the South China Sea along the Manila trench and collision with Taiwan Island

92 (Lüdmann et al., 2001), convective removal of continental lithosphere by warm asthenosphere

93 (Lester et al., 2014), or magma ascent from a high-velocity layer in the lower crust fed by the Hainan

94 mantle plume (Xia et al., 2016; Fan et al., 2017). Volcanoes generated by post-rift magmatism in

95 the early Miocene and Quaternary were emplaced both onshore and offshore (e.g. Zou et al., 1995;

96 Yan et al., 2006; Franke, 2013; Li et al., 2014; Sun et al., 2014b; Zhao et al., 2014, 2016; Fan et al.,

97 2017), with the latter typically extruded onto the continental slope in relatively shallow water depths

98 (<300 m; Yan et al., 2006; Zhao et al., 2016). Boreholes reveal these shallow-water volcanoes are

99 composed of basalt, dacite, and rhyolitic tuff (Li and Liang, 1994; Yan et al., 2006; Zhao et al.,

100 2016). In addition to the onshore and shallow-water volcanoes, several volcanoes were emplaced

101 further basinwards on the continental slope in deeper water, close to the Continent-Ocean Boundary

102 (COB) (Clift et al., 2001; Wang et al., 2006; Cameselle et al., 2017) (Fig. 1). We examine two of

103 these deep-water volcanoes, which are situated in an area currently characterized by water depths

104 of 1850–2680 m and that are now buried by sedimentary strata up to 330 m thick (Fig. 1).

105 Micropalaeontological data from the Pearl River Mouth Basin (Xu et al., 1995; Qin, 1996), and

106 microfauna data from ODP sites 1146 and 1148, indicate the Middle Miocene (16.5 Ma) to Recent,

107 nanofossil-bearing clays enclosing the volcanoes were deposited in a deep-water setting (1.0–3.0 km;

108 Wang et al., 2000).

109

110 **3. Data and Methods**



111 We use a time-migrated 3D seismic reflection survey acquired in 2012 and covering an area of  
112  $\sim 350 \text{ km}^2$  (Fig. 1b). The seismic data are zero-phase processed and displayed with SEG (Society of  
113 Exploration Geophysicists) normal polarity, whereby a downward increase in acoustic impedance  
114 (a function of rock velocity and density) corresponds to a positive reflection event (red on seismic  
115 profiles) (e.g. Brown, 2004). Bin spacing is 25 m, and the seismic data have a dominant frequency  
116 in the interval of interest (i.e. 0–400 ms two-way time (tw)) of  $\sim 40 \text{ Hz}$ .

117 Stacking velocities are not available for the survey and no wells intersect the studied Late  
118 Miocene-Quaternary, buried, deep-water volcanic features. We thus have no direct control on the  
119 composition or velocities of the seismically imaged volcanic materials. Depth-conversion of  
120 volcanic and lava flow thickness measurements in milliseconds (tw) to meters is therefore based on  
121 velocity estimates, which introduces some uncertainty into our erupted volume calculations. To  
122 derive a reasonable velocity estimate, we use velocity data for submarine volcanoes obtained from  
123 boreholes (i.e. BY7-1 and U1431) (Li et al., 2015; Zhao et al., 2016) and OBS (Ocean Bottom  
124 Seismometer) profiles (Yan et al., 2001; Wang et al., 2006; Chiu, 2010; Wei et al., 2011) in the  
125 South China Sea. The boreholes, which are situated  $>300 \text{ km}$  away from our study area, intersect  
126 buried basaltic volcanoes with p-wave velocities of  $\sim 4.5 \text{ km/s}$  (BY7-1; Zhao et al., 2016) and  $\sim 3.0$ –  
127  $5.0 \text{ km/s}$  (IODP U1431; Li et al., 2015). OBS profiles reveal submarine volcanoes located 140 km  
128 from the study area (Fig. 1a) typically have p-wave velocities of  $>3.0 \text{ km/s}$ , and occasionally up to  
129  $\sim 5.5 \text{ km/s}$  (Yan et al., 2001; Wang et al., 2006; Chiu, 2010; Wei et al., 2011). The basaltic  
130 composition and p-wave velocities of  $\sim 3.0$ – $5.5 \text{ km/s}$  for volcanoes intersected by boreholes and  
131 studied using OBS data are consistent with p-wave velocity data for shallow-water, mafic volcanoes  
132 located offshore western India ( $\sim 3.3$ – $5.5 \text{ km/s}$ ; Calvès et al., 2011), and southern Australia in the



133 Bight (~2.4–6.7 km/s, with an average velocity of 4.0 km/s; Magee et al. 2013) and Bass (~2.2–4.0  
134 km/s with an average of 3.0 km/s; Reynolds et al. 2018) basins. Based on these velocity data, we  
135 assume the imaged volcanic ~~material studied~~ here have mafic compositions and p-wave velocities  
136 of 4.0 ( $\pm 1.0$ ) km/s. It is important to note that using a range of estimated velocities does not affect  
137 our calculation of the *relative* amount of material contained within volcanic edifices versus the  
138 flanking lava flows.

139 We calculate a vertical resolution ( $\lambda/4$ ) of ~10 m for the sedimentary strata ~~encasing~~ the volcanic  
140 materials, given a dominant frequency of 40 Hz and assuming a seismic velocity of 2.2 km/s for the  
141 nanofossil-bearing clay (based on seismic refraction profiles OBS1993, Yan et al., 2001; OBS2001,  
142 Wang et al., 2006; OBS2006-3, Wei et al., 2011). The calculated vertical resolution for the volcanic  
143 materials is 19–31 m, based on a dominant frequency of 40 Hz and estimated seismic velocities of  
144 4.0 ( $\pm 1.0$ ) km/s. The top and base of volcanic structures can be distinguished in seismic reflection  
145 data when their thickness is greater than the estimated vertical resolution ~~of these data~~ (i.e. 19–31  
146 m) (Brown, 2004). Volcanic structures with thicknesses below the vertical resolution, but above the  
147 detection limit (i.e.  $\lambda/8 = 10$ –16 m), are imaged as tuned reflection packages whereby reflections  
148 from their top and base contacts interfere on their return to the surface and cannot be distinguished  
149 (Brown, 2004). The lava flows ~~are~~ typically >2 seismic reflection thick ( $>4 \pm 10$  m), suggesting  
150 they too are thicker than the tuning thickness and are represented by discrete top and basal  
151 reflections (Tables 1-3).

152 We used a regional 2D seismic profile and interpreted four seismic ~~surfaces~~ tied to ODP Site 1146,  
153 which is located ~65 km west of the study area (Figs. 1a, 2), and two horizons locally mappable  
154 around the volcanoes: T0 (~2.58 Ma), T1 (~5.3 Ma), TRa (~6.5 Ma), and TRb (~8.2 Ma), TM (top



155 of the volcanic material) and BM (base of the volcanic material). The youngest age of the volcanoes  
156 and associated lava flows are determined using the first seismic reflection that onlaps or overlies  
157 them (Fig. 3). After mapping TM and BM, we calculated the volumes of the volcanic features  
158 (Tables 1-4), with errors largely arising from uncertainties in the velocities ( $4.0 \pm 1.0$  km/s) used to  
159 undertake the depth conversion (see above).

160 Root mean square (RMS) amplitude extractions and slices through a variance volume were used  
161 to constrain the geometry, scale, and distribution of the submarine volcanoes (Figs. 3-8). The RMS  
162 amplitude attribute computes the square root of the sum of squared amplitudes, divided by the  
163 number of samples within the specified window used; put simply, the RMS attribute measures the  
164 reflectivity of a given thickness of seismic data (Fig. 4a) (Brown, 2004). The variance attribute is  
165 free of interpreter bias because it is directly derived from the processed data (Fig. 5). Variance  
166 measures the variability in shape between seismic traces; this can be done in a specified window  
167 along a picked horizon or within a full 3D seismic volume. Variance is typically used to map  
168 structural and stratigraphic discontinuities related to, for example, faults and channels (Brown,  
169 2004).

170

## 171 **4. Seismic expression and interpretation of igneous features**

172

### 173 **4.1. Observations**

174 We identify three main types of seismic structures and associated facies: (1) Seismic Facies 1  
175 (SF1) - two (V1 and V2) conical-shaped features up to ~202 ms twt (~404±101 m) thick, which  
176 internally are weakly-to-moderately reflective or chaotic with distinguished reflections





177 downlapping onto BM, capped by a positive polarity, high-amplitude reflection (TM) overlapped by  
178 overlying strata (Figs. 3a, 7); (2) Seismic Facies 2 (SF2) - ribbon-like, broadly strata-concordant,  
179 high-amplitude, positive polarity reflections, which emanate from the conical structures (SF1) and  
180 extend up to ~9.2 km downslope (Figs. 3a-b, 6-7); and (3) Seismic Facies 3 (SF3) - saucer-shaped,  
181 strata-discordant, high-amplitude reflections situated beneath SF1 and SF2 (Fig. 6).

182

## 183 4.2. Interpretations

184 The conical shape of SF1 and downlap of its internal reflections (where developed) onto BM,  
185 coupled with onlap of overlying reflections onto TM, suggest SF1 is an extrusive rather than  
186 intrusive feature. SF1 is similar in terms of its conical shape, highly reflective top, and internally  
187 chaotic reflections to mud volcanoes documented elsewhere in the northern South China Sea (Sun  
188 et al., 2012; Yan et al., 2017). It is therefore plausible SF1 could represent a mud volcano that fed  
189 long run-out mud flows (i.e. SF2). Alternatively, the highly reflective, ribbon-like geometry of SF2  
190 is similar to that associated with shallow/free gas accumulations (Sun et al., 2012). We consider  
191 these two interpretations unlikely because: (i) the limited supply and high viscosity of mud means  
192 mud volcanoes are rarely associated with long run-out flows, although we note that one mud flow  
193 in the Indus Fan was ~5.0 km long (Calvès et al. 2009); and (ii) the top of SF2 is defined by a  
194 positive polarity reflection (downward increase in acoustic impedance), which is opposite to that  
195 typically associated with shallow/free gas accumulations (e.g. Judd and Hovland, 2007; Sun et al.,  
196 2012). Based on their geometric and geophysical characteristics, spatial relationships, and similarity  
197 to structures observed on other rifted continental margins, we interpret these features as volcanic  
198 edifices (SF1), genetically related lava flows (SF2), and saucer-shaped gills (SF3) (e.g. Berndt et al.,



199 2000; Planke et al., 2000; Thomson and Hutton, 2004; Calvès et al., 2011; Jackson, 2012; Magee et  
200 al., 2013; Reynolds et al., 2018). We now focus on the detailed external morphology and internal  
201 architecture of the two deep-water volcanoes that are shallowly buried ( $<330$  m) and thus well-  
202 imaged.

203

#### 204 4.3. Volcano edifice 1 (V1) and associated lava flows

205 V1 is a prominent,  $\sim 202$  ms twt high ( $404 \pm 101$  m) and  $\sim 3.0$  km diameter conical volcano covering  
206  $\sim 7.2$  km<sup>2</sup>, with a volume of  $\sim 0.94 \pm 0.24$  km<sup>3</sup> and an average flank dip of  $\sim 15.0 \pm 3.6^\circ$  (Figs. 3-4;  
207 Table 1). V1 is overlapped by overlying reflections, with the oldest overlapping reflection correlating  
208 to TRa ( $\sim 6.5$  Ma); this suggests V1 was emplaced in the latest Miocene-earliest Pliocene (Fig. 3a).  
209 V1 is underlain by a downward-tapering,  $>1.1$  km deep, up to 2.0 km wide, sub-vertical zone of  
210 chaotic reflections (Fig. 3a). We attribute the poor imaging within this chaotic sub-vertical zone to:  
211 (1) the presence of sub-vertical feeder intrusions that disrupt background reflections and scatter  
212 energy (cf. Thomson, 2007); (2) increased fluid flow and hydrothermal alteration in fractured and  
213 deformed host rock adjacent to the magma plumbing system; and/or (3) scattering of energy  
214 travelling through the volcano, leading to ‘wash-out’ of the underlying data (i.e. a geophysical  
215 artefact; Magee et al. 2013). This reduction in imaging beneath the volcanoes partly obscures their  
216 basal surface, but where visible it is clear BM undulates and truncates underlying stratal reflections  
217 (Fig. 3b).

218 Volcano V1 is surrounded by an asymmetric apron of moderate-to-high amplitude reflections  
219 extending up to 1.5 km from the main edifice. The apron is up to  $\sim 115$  ms twt thick ( $\sim 230 \pm 58$  m),  
220 and has a dip of  $<0.5^\circ$  (Figs. 4a-b; Table 2). A package of moderate-to-very high-amplitude



221 reflections extending a further c. 1.5 km down-dip of this apron contains very high-amplitude,  
222 channel-like geometries (marked ~~with~~ C1-C3 in (Fig. 4a), which terminate down-dip into or are  
223 flanked at prominent bends by, moderate-amplitude, fan-like geometries (marked ~~with~~ F1-F4 in Fig.  
224 4a). We interpret these two features as lava flow channels and fans, respectively (Fig. 3-4). The lava  
225 flow channels are sinuous, <340 m wide, and usually bisect the lava fans (Figs 4a-b). Lava flow-  
226 related features (i.e. apron, channels, and fans) emanating from V1 cover an area of  $\sim 14 \text{ km}^2$  (Tables  
227 3-4), have an average thickness of  $\sim 33 \text{ ms twt}$  ( $\sim 66 \pm 17 \text{ m}$ ), and a volume of  $\sim 0.92 \pm 0.23 \text{ km}^3$ ; this  
228 volume is nearly equal to that of V1 ( $\sim 0.94 \pm 0.24 \text{ km}^3$ ) and thus represents  $\sim 50\%$  of the total erupted  
229 volume ( $\sim 1.86 \pm 0.47 \text{ km}^3$ ).

230

#### 231 4. 4. Volcano edifice 2 (V2) and associated lava flows

232 V2 covers  $\sim 0.44 \text{ km}^2$  and is elliptical in plan-view, with long and short axes of  $\sim 1.2 \text{ km}$  and  $\sim 0.6$   
233 km, respectively (Figs. 5, 7). The volcano is  $\sim 100 \text{ ms twt}$  high ( $\sim 200 \pm 50 \text{ m}$ ), with an irregular base,  
234 has flank dips of  $\sim 27.8 \pm 5.9^\circ$ , and a volume of  $0.03 \pm 0.01 \text{ km}^3$  (Figs. 5, 7; Table 1). The top of V2 is  
235 of moderate amplitude and is irregular, with the oldest onlapping reflections correlating to Reflector  
236 T1 ( $\sim 5.3 \text{ Ma}$ ) suggesting V2 is latest Miocene-earliest Pliocene, but probably younger than V1 (Fig.  
237 7). Reflections within V2 are chaotic and, similar to V1, V2 is underlain by a vertical zone of  
238 disturbance (Fig. 7). V2 lacks a lava apron, instead being directly flanked by relatively straight, up  
239 to 9.2 km long lava flow channels on its south-eastern side (C4-C7) (Fig. 5a). Lava flow C6 is  
240 unusual in that underlying strata are truncated at the base of the flow, defining ‘ramps’ that are up  
241 to  $\sim 32.5 \text{ ms twt}$  high ( $\sim 65 \pm 16 \text{ m}$ ) ~~high~~ and dip towards V2 at  $\sim 25.5 \pm 5.8^\circ$  (Fig. 8). Beyond the main  
242 ramp at the base of lava flow C6 (Fig. 5b), the lava flows thicken to  $\sim 130 \text{ ms twt}$  ( $\sim 260 \pm 65 \text{ m}$ ),



243 where it is defined by stacked, high-amplitude reflections that have a lobate geometry in plan-view  
244 (F5) (Figs. 5, 7, 8c-d). At its distal end, the pinch out of F5 occurs where it abuts a basal ramp that  
245 is  $\sim 90 \pm 23$  m tall and that dips  $\sim 9.3 \pm 2.3^\circ$  (Figs. 8c-d). F5 is capped by a younger lava fan (F6) (Figs.  
246 8c-d). The V2-sourced lava flows (C4-C7 and F5) cover  $\sim 11.5$  km<sup>2</sup>;  $\sim 4.20$  km<sup>2</sup> of this comprises  
247 lava flow channels and  $\sim 7.32$  km<sup>2</sup> lava fan. Given the average thickness of the lava flow channels  
248 ( $\sim 61 \pm 16$  m) and fans ( $\sim 109 \pm 27$  m), we estimate the total volume of V2-sourced lava flows to be  
249  $\sim 1.05 \pm 0.27$  km<sup>3</sup>; this volume estimate is  $\sim 35$  times greater than that of the main V2 edifice  
250 ( $0.03 \pm 0.01$  km<sup>3</sup>), representing  $\sim 97\%$  of the total erupted volume.

251

#### 252 4.5. Shallow sills and associated lava flows

253 South of V2, we map two areally extensive, partly merged lava flows emanating from the upper  
254 tips of inclined sheets fringing saucer-shaped sills (i.e. S1 and S2) (Figs. 1b, 5-6). A narrow, vertical,  
255 seismically chaotic/blanking zone occurs directly below the saucer-shaped sills (Fig. 6). Several  
256 linear structures, rooted at the junction between sills, and feeding the overlying lava fan (F6), are  
257 also observed (Fig. 6). F6 covers an area of  $\sim 49$  km<sup>2</sup>, with a diameter of  $\sim 7.9$  km and thickness of  
258  $55 \pm 14$  m (Table 4). F6 is directly onlapped by surface T0 ( $\sim 2.58$  Ma), suggesting it was emplaced  
259 in the latest Pliocene (Fig. 6). Similar to other lava fans, F6 is characterized by a single, positive,  
260 high-amplitude seismic event (Fig. 6). F6 extends beyond the seismic coverage and is much bigger  
261 than other lava fans imaged in the study area (Figs. 5-6; Table 4).

262

### 263 5. Discussion

#### 264 5.1. Water depths during volcano emplacement



265 The different burial depths and onlap relationships of the volcano edifices and lava flows studied  
266 here suggest three phases of volcanism: i.e. ~6.5 Ma for V1, ~5.3 Ma for V2, and ~2.58 Ma for  
267 S1/S2 (Figs. 2-3, 6-7). According to the relative sea-level change curve of the Pearl River Mouth  
268 Basin acquired from nannofossils (Xu et al., 1995; Qin, 1996) and the dating of volcanic phases, the  
269 water depths during V1 and V2 emplacement were likely ~75 m and ~150 m shallower than the  
270 present depths of ~2.25 km and ~2.14 km, respectively. The water depth during the emplacement of  
271 F6, fed by S1/S2, was probably ~150 m greater than the present depth of ~2.32 km (Xu et al., 1995;  
272 Qin, 1996). To be conservative, we estimate that volcanism in the study area occurred in water  
273 depths of a little over 2.0 km.

274

## 275 5.2. Origin of post-spreading volcanism in the SCS

276 The volcanoes documented here (~6.3–2.58 Ma) have similar ages with those documented ~~in the~~  
277 Hainan Island (e.g. Tu et al., 1991; Shi et al., 2011) and southwestern SCS (e.g. Li et al., 2013) (Fig.  
278 1a). However, ~~our~~ volcanoes are substantially younger than those previously observed in the central  
279 SCS (~13.8–7.0 Ma; Expedition 349 Scientists, 2014; Li et al., 2015) and on the middle-lower slope  
280 of the northern SCS (~23.8–17.0 Ma; Yan et al., 2006; Zhao et al., 2016; Fan et al., 2017). We note  
281 ~~such~~ small-scale, buried, post-spreading volcanic features studied here have not been identified by  
282 lower-resolution techniques (e.g. gravity, magnetism, OBS and 2D seismic data). These young  
283 volcanic features ~~maybe~~ widespread and diagnostic of post-spreading magmatism across the  
284 northern SCS (e.g. Briais et al., 1993; Yan et al., 2006).

285 Given that the volcanoes documented here were emplaced after SCS rifting (>32 Ma ago; e.g.  
286 Taylor and Hayes, 1983; Franke et al., 2014; Li et al., 2015) and spreading (>15 Ma ago; Li et al.,



287 2014), it is clear they have a different origin to the breakup-related volcanoes described elsewhere  
288 (e.g. Yan et al., 2006; Expedition 349 Scientists, 2014; Li et al., 2015; Zhao et al., 2016; Fan et al.,  
289 2017). The post-spreading age of volcanism may suggest that mantle melting (Clift et al., 2001) and  
290 convective removal of continental lithosphere by warm asthenosphere (Lester et al., 2014),  
291 processes typically associated with rifting and breakup, were not responsible for the generation of  
292 this phase of igneous activity. Magmatism gets younger south-eastwards, from ~23.8–17.0 Ma on  
293 the proximal continental slope (Yan et al., 2006; Zhao et al., 2016; Fan et al., 2017) to ~6.30–2.58  
294 Ma in the deeper water study area. This observation is seemingly in agreement with the results of  
295 teleseismic imaging, which shows southeastward migration of the eastern branch of the Hainan  
296 mantle plume (Xia et al., 2016). This suggests that plume melt (Xia et al., 2016; Fan et al., 2017)  
297 may have supplied magma to the observed volcanoes. However, where the Hainan mantle plume  
298 was located or even whether the Hainan mantle plume occurred or not are still questioned at present  
299 (e.g. Wheeler and White, 2000; He and Wen, 2011; Zhang and Li, 2018). Another possibility for  
300 the origin of magma is related to the Dongsha Event that likely triggered the upwelling of mantle  
301 materials as well as transtensional faulting (Lüdmann et al., 1999). The Dongsha Event peaked at  
302 ~5.3 Ma and 2.58 Ma (Lüdmann et al., 2001) and was broadly synchronous with the main period of  
303 eruptive magmatism documented here. Faults generated during the Dongsha Event may have  
304 provided high-permeability zones that promoted the vertical migration of magma that fed the  
305 eruptive centers.

306

### 307 5.3. Volcano construction

308 Both V1 and V2 are underlain by sub-vertical, pipe-like zones of chaotic reflections, which we



309 suggest demarcate the limits of their magma plumbing systems. The basal surfaces of V1 and V2  
310 truncate underlying strata (Figs. 3a, 7). Apparent erosion of the sub-volcanic substrate may indicate  
311 the initial eruptions were explosive, ~~similar to eye-shaped hydrothermal vents documented by, for~~  
312 ~~example, Hansen et al. 2006; Magee et al. 2016).~~ Alternatively, subsidence of the volcano load into  
313 underlying, wet, unconsolidated sediments may have caused the strata to locally compact and  
314 thereby change the reflection configuration, making it appear that they are truncated.

315 Internal reflections that lie sub-parallel to the flanks of V1 and V2 suggest the volcanoes grew by  
316 increasing both edifice height and diameter by the accretion of volcanic material (Magee et al. 2013).  
317 Flank dips of  $\sim 15\text{--}28^\circ$  likely indicate that the volcanic material building the edifices constitutes  
318 coherent lava flows and/or a dome structure, rather than a pyroclastic cone of tephra (Francis and  
319 Thorpe, 1974; Griffiths and Fink, 1992). Construction via emplacement of coherent lava flows is  
320 consistent with the presence of internal reflections in V1 and V2; i.e. boundaries between blocky  
321 lava flows would be irregular and scatter seismic energy, meaning they would not likely be imaged.  
322

#### 323 5.4. Lava flow extrusion dynamics

324 In addition to the formation of volcanic edifices, both V1 and V2, as well as S1 and S2, are  
325 associated with extensive lava flows. In particular, we show V1 and V2 are flanked either by an  
326 asymmetric lava apron, which is broader on their downslope (SE) side, or lava flow channels that  
327 flowed south-eastwards for up to  $>9$  km (Figs. 3a, 4a-b, 5a). At sub-aerial volcanoes (e.g. Walker,  
328 1993; Cashman et al., 1999), high eruption rates and low magma viscosities are the dominant causes  
329 of long run-out lava flows. Extensive lava flows have also been observed at other deep-water  
330 volcanoes and occur primarily because of the high hydrostatic pressure in deep-water environments



(e.g. Chadwick et al., 2018; Embley and Rubin, 2018; Ikegami et al., 2018). In particular, higher ambient pressure can affect lava rheology (lower viscosity, vesicularity, crystal content), suppress magma decompression and ascent, and, thereby, extrusion dynamics (Bridges, 1997; Gregg and Fornari, 1998). For example, upon eruption of a 1200–1100°C basalt (MORB composition) at a confining pressure of 20 MPa (i.e. a hydrostatic-equivalent water depth of 2 km), lava can contain up to 1.4 wt% H<sub>2</sub>O at equilibrium volatile solubility (Newman and Lowenstern, 2002). The resulting lava viscosity of 9–38 Pa s is significantly lower than a dry (0.1 wt% H<sub>2</sub>O) sub-aerial basalt, having a viscosity range of 41–248 Pa s (calculated using Giordano et al., 2008). Higher H<sub>2</sub>O content in lavas erupted in deep-water, compared to those extruded in sub-aerial settings, will mean: (1) there are fewer bubbles from suppressed degassing or brittle fragmentation to hinder flow (Gregg and Fornari, 1998); (2) crystallization may be inhibited, reducing the effect of crystal interactions on viscosity; and (3) the glass transition temperature is suppressed (Giordano et al. 2008), allowing lavas to flow further.

From our seismic reflection data it is also clear channelization in lava tubes, in addition to the water content effects described above, also facilitated long distance lava transport. We suggest these tubes formed by rapid cooling and hardening of a surficial crust that insulated and focused lava flow through a core channel (e.g. Cashman et al., 1999). Based on the long run-out lava distances, we consider our initial assumption that the imaged volcanic features have a mafic composition remains valid. Overall, whilst we do not know the composition of the lavas imaged in our seismic reflection data, pressure-related changes in lava rheology and channelization of any lava type (i.e. mafic to silicic) will allow it to flow hotter for longer. Given the downslope topographic controls during eruption, a combination of rheology changes and channelization allowed lavas to flow for >9 km





353 from associated volcanic edifices.

354 The overall geometry and internal architecture of the imaged lava flows indicate substrate  
355 rheology was a ~~key~~ control on emplacement dynamics. Our 3D seismic reflection data show that  
356 relatively long run-out lava flows (>9 km) erupted from deep-water volcanoes have a rugged basal  
357 surface that is locally defined by erosional basal 'ramps'. Truncation of underlying strata suggests  
358 the lavas were able to erode down into the seabed, perhaps because the pre-eruption substrate was  
359 cold, wet, and unconsolidated. We suggest erosion of the lava substrate was promoted by: (1) the  
360 dense (bubble-poor) lava sinking down into or 'dredging' the soft sediments (Duffield et al., 1986;  
361 Ikegami et al. 2018); (2) thermal erosion (Griffiths, 2000); and/or (3) more "turbulent" flow  
362 dynamics of channelized lava, consistent with the inferred low viscosities (<10 Pa s).

363 Lava flows eventually ceased in distal areas due to gradual cooling and crystallization (Cashman  
364 et al., 1999). We suggest that, in the case of the straight lava flows (C5 and C6), lava transported  
365 within the axial tube temporarily accumulated at the ~~transient~~ end of the flow, ~~possibly forming a~~  
366 ~~lava pool (Greeley, 1987)~~. Lava entering the tube from the ongoing ~~or new~~ volcanic eruption caused  
367 an increase in pressure, with the cooled and crystallized material at the flow toe forming an  
368 ~~impermeable, albeit, transient barrier. High hydrostatic pressure (>26 MPa at C5 and C6) and thick~~  
369 ~~surfacial crusts inhibited the release of pressure build-up by significant lava inflation (Gregg and~~  
370 ~~Fornari, 1998)~~. Eventually, pressure build-up was sufficient to rupture this frontal ~~l~~ leading to  
371 emplacement of a fan downdip of the ~~front-most base-lava ramp~~ (F5; Fig. 5a, 7-8) (Griffiths, 2000).  
372 However, in the case of fans (e.g. F1-4) fed by sinuous channels (Figs. 4a-b), we suggest these were  
373 emplaced in a process similar to that documented by Miles and Cartwright (2010), with lobate lava  
374 flows fed and bisected by a 'lava tube' through magma inflation and increases in eruption rate. At



the end of sinuous lava flow channels (e.g. C1), the main channel bifurcated to form a lobate fan (F3, Figs. 4a-b), which was also probably caused by flow branching triggered by magma cooling (Griffiths, 2000).

378

### 379 5.5. Volume balance of volcano edifice and lava flow

Inaccurate constraints on total erupted volumes ~~compromises~~ our understanding of volcano construction, lava propagation, eruption rates, eruption durations, magma storage conditions, melting processes, and risk assessment of volcanism in deep-water settings (Carey et al., 2018).

High-resolution 3D seismic reflection data allow us to calculate the volumes of material contained within volcano edifices and in flanking lava flows. We show that most (i.e. 50-97%) of the erupted material ~~is~~ transported away from the imaged edifices, ~~an observation comparable to that made for~~

~~deep-ocean volcanic eruptions (Caress et al., 2012; Carey et al., 2018). A critical outcome~~ of our work is that flanking lava flows, and to a lesser extent the volcanic edifices, have rugged and discordant bases (Fig. 7); accurately calculating the volume of deep-water volcanoes and lava flows

therefore requires an understanding of their basal morphology. Erupted volume estimates based solely on remote sensing of the seabed may be thus incorrect (e.g. Robinson and Eakins, 2006).

Although we show the accuracy of total erupted volume estimates can be improved by constraining basal volcano and lava morphologies, seismic images capturing the geological record of deep-water volcanoes cannot determine how much, if any, volcanic material was transported away from the

eruption site as pumice rafts (e.g. Carey et al. 2018). Nevertheless, 3D seismic imaging can significantly improve quantitative volume estimates of recent and ancient ~~volcanic features (e.g.~~

volcano edifices and lava flows) either ~~currently~~ on the seafloor or ~~now~~ buried by sedimentary





397 successions.

398

## 399 6. Conclusions

400 High-resolution 3-D seismic data from the South China Sea allow us to image and map the  
401 internal structure, calculate the volume of erupted material, and to better understand the extrusion  
402 dynamics of buried deep-water volcanoes; such insights cannot readily be gained from analysis of  
403 **remote sensing data**. Volcanism occurred ~6.3–2.58 Ma, after seafloor spreading had ceased in the  
404 area, and may be related to the Dongsha Event and/or a hypothesized Hainan mantle plume. High  
405 hydrostatic pressure, an inclined seabed (~1°), and low-strength, very fine-grained, near-seabed  
406 sediments, combined with formation of lava tubes and extrusion of low-viscosity magmas, are likely  
407 responsible for observed long-distance lava run-outs (>9 km) in this deep-water environment. We  
408 show the imaged volcanic edifices and associated lava flows have rugged, erosional bases, ~~meaning~~  
409 ~~traditional remote sensing-based volume calculations of deep-water volcanic features, which~~  
410 ~~typically assume smooth bases, are underestimated. Because seismic reflection data images the base~~  
411 ~~of deep-water volcanoes and lava flows, we~~ calculate a large amount (as high as ~97%) of the  
412 erupted materials ~~are~~ transported away from the volcano edifices, ~~suggesting that volume of deep-~~  
413 ~~water volcanic edifices may not faithfully archive eruption size or magma production.~~ Considering  
414 deep-water conditions (e.g. high hydrostatic pressure and unconsolidated sediments) in the study  
415 area are common elsewhere, the conclusions derived from this study can likely be used in other  
416 deep-water sedimentary basins and ~~some~~ mid-ocean ridges. Our study highlights that 3D seismic  
417 reflection data can ~~play a critical~~ to understanding volcano morphology in 3D and accurately  
418 estimating ~~volumes~~ of erupted material.



419

## 420 **Author Contribution**

421 Qiliang Sun, Christopher A-L. Jackson, Craig Magee and Xinong Xie have contributed to the  
422 conceptualization, data analysis, writing and revising the original draft. Samuel J. Mitchell ~~have~~  
423 contributed to the conceptualization and revising the original draft.

424

## 425 **Competing interests**

426 The authors declare that they have no conflict of interest.

427

## 428 **Acknowledgment**

429 This work was supported by the National Scientific Foundation of China (Grant Nos. 91528301,  
430 41676051 and 41372112), the Programme of Introducing Talents of Discipline to Universities (No.  
431 B14031) and the Fundamental Research Funds for the Central Universities-the China University of  
432 Geosciences (Wuhan) (No. CUG160604). We thank the China National Offshore Oil Company  
433 (CNOOC) for permission to release the data; reflection seismic data may be requested from CNOOC  
434 (<http://www.cnooc.com.cn/en/>). Dieter Franke, Gerome Calvès and Nick Schofield are thanked for  
435 their invaluable comments and suggestions. Rebecca Bell is thanked for generously providing office  
436 space during the visit of Qiliang Sun to Imperial College.

437

## 438 **References**

439 Allen, R.W., Berry, C., Henstock, T.J., Collier, J.S., Dondin, F.J-Y., Rietbrock, A., Latchman, J.L., and Robertson,  
440 R.E.A.: 30 Years in the Life of an Active Submarine Volcano: A Time - Lapse Bathymetry Study of the Kick-em-



- 441 Jenny Volcano, Lesser Antilles, *Geochem. Geophys. Geosy.*, 19, 715-731, <https://doi.org/10.1002/2017GC007270>,  
442 2018.
- 443 Berndt, C., Skogly, O.P., Planke, S., Eldholm, O., and Mjelde, R.: High-velocity break up-related sills in the Vøring  
444 Basin, off Norway, *J. Geophys. Res.*, 105, 28443-28454, <https://doi.org/10.1029/2000JB900217>, 2000.
- 445 Briaies, A., Patriat, P., and Tapponnier, P.: Updated interpretation of magnetic anomalies and seafloor spreading stages  
446 in the South China Sea: Implications for the Tertiary tectonics of Southeast Asia, *J. Geophys. Res.*, 98, 6299-6328,  
447 <https://doi.org/10.1029/92JB02280>, 1993.
- 448 Bridges, N.T.: Ambient effects on basalt and rhyolite lavas under Venusian, subaerial, and subaqueous conditions, *J.*  
449 *Geophys. Res.*, 102(E4), 9243-9255, <https://doi.org/10.1029/97JE00390>, 1997.
- 450 Brown, A.R.: Interpretation of three-dimensional seismic data: AAPG Memoir 42, 6thed. SEG Investigations in  
451 Geophysics, 2004.
- 452 Calvès, G., Schwab, A.M., Huuse, M., Clift, P.D., Gaina, C., Jolley, D., Tabrez, A.R., and Inam, A.: Seismic  
453 volcanostratigraphy of the western Indian rifted margin: The pre-Deccan igneous province, *J. Geophys. Res.*, 116,  
454 B01101, <https://doi.org/10.1029/2010JB000862>, 2011.
- 455 Calvès, G., Schwab, A.M., Huuse, M., van Rensbergen, P., Clift, P.D., Tabrez, A.R., and Inam, A.: Cenozoic mud  
456 volcano activity along the Indus Fan: offshore Pakistan, *Basin Res.*, 22, 398-413, [https://doi.org/10.1111/j.1365-](https://doi.org/10.1111/j.1365-2117.2009.00448.x)  
457 2117.2009.00448.x, 2009.
- 458 Cameselle, A.L., Ranero, C.R., Franke, D., and Barckhausen, U.: The continent-ocean transition on the northwestern  
459 South China Sea, *Basin Res.*, 29, 73-95, <https://doi.org/10.1111/bre.12137>, 2017.
- 460 Caress, D.W., Clague, D.A., Paduan, J.B., Martin, J.F., Dreyer, B.M., Chadwick Jr, W.W., Denny, A., and Kelley,  
461 D.S.: Repeat bathymetric surveys at 1-metre resolution of lava flows erupted at Axial Seamount in April 2011,  
462 *Nat. Geosci.*, 5, 483-488, <https://doi.org/10.1038/NGEO1496>, 2012.



- 463 Carey, R., Soule, S.A., Manga, M., White, J.D.L., McPhie, J., Wysoczanski, R., Jutzeler, M., Tani, K., Yoerger, D.,  
464 Fornari, D., Caratori-Tontini, F., Houghton, B., Mitchell, S., Ikegami, F., Conway, C., Murch, A., Fauria, K., Jones,  
465 M., Cahalan, R., and McKenzie, W.: The largest deep-ocean silicic volcanic eruption of the past century, *Sci. Adv.*,  
466 4, e1701121, <https://doi.org/10.1126/sciadv.1701121>, 2018.
- 467 Cashman, K.V., Thornber, C.R., and Kauahikaua, J.P.: Cooling and crystallization of lava in open channels, and the  
468 transition of pahoehoe lava to 'a'a, *B. Volcanol.*, 61, 306-323, <https://doi.org/10.1007/s004450050>, 1999.
- 469 Chadwick Jr, W.W., Merle, S.G., Baker, E.T., Walker, S.L., Resing, J.A., Butterfield, D.A., Anderson, M.O.,  
470 Baumberger, T. and Bobbitt, A.M.: A recent volcanic eruption discovered on the central Mariana back-arc  
471 spreading center: *Front. Earth Sci.*, 6, 172, <https://doi.org/10.3389/feart.2018.00172>, 2018.
- 472 Chiu, M.: The p-wave velocity modeling of the transitional crust in northern South China Sea continental margin,  
473 M.S. dissertation, National Taiwan Ocean University, Keelung, 112 pp., 2010.
- 474 Clift, P.D., Lin, J., and ODP Leg 184 Scientific Party: Patterns of extension and magmatism along the continent-  
475 ocean boundary, South China margin, Geological Society, London, Special Publications, 187, 489-510,  
476 <https://doi.org/10.1144/GSL.SP.2001.187.01.24>, 2001.
- 477 Cocchi, L., Masetti, G., Muccini, F., and Carmisciano, C.: Geophysical mapping of Vercelli Seamount: Implications  
478 for Miocene evolution of the Tyrrhenian back arc basin, *Geosci. Front.*, 7, 835-849,  
479 <https://doi.org/10.1016/j.gsf.2015.06.006>, 2016.
- 480 Ding, W.W., and Li, J.B.: Propagated rifting in the Southwest Sub-basin, South China Sea: Insights from analogue  
481 modelling, *J. Geodyn.*, 100, 71-86, <https://doi.org/10.1016/j.jog.2016.02.004>, 2016
- 482 Duffield, W.A., Bacon, C.R., and Delaney, P.T.: Deformation of poorly consolidated sediment during shallow  
483 emplacement of a basalt sill, Coso Range, California, *B. Volcanol.*, 48, 97-107,  
484 <https://doi.org/10.1007/BF01046545>, 1986.



- 485 Embley, R.W. and Rubin, K.H.: Extensive young silicic volcanism produces large deep submarine lava flows in the  
486 NE Lau Basin, B. Volcanol., 80, 36, <https://doi.org/10.1007/s00445-018-1211-7>, 2018.
- 487 Expedition 349 Scientists: South China Sea tectonics: Opening of the South China Sea and its implications for  
488 southeast Asian tectonics, climates, and deep mantle processes since the late Mesozoic, International Ocean  
489 Discovery Program Preliminary Report, 349, <https://doi.org/10.14379/iodp.pr.349.2014>, 2014.
- 490 Fan, C.Y., Xia, S.H., Zhao, F., Sun, J.L., Cao, J.H., Xu, H.L., and Wan, K.Y.: New insights into the magmatism in  
491 the northern margin of the South China Sea: Spatial features and volume of intraplate seamounts, Geochem.  
492 Geophys. Geosy., 18, 2216-2239, <https://doi.org/10.1002/2016GC006792>, 2017.
- 493 Francis, P.W. and Thorpe, R.S.: Significance of lithologic and morphologic variations of pyroclastic cones, Geo. Soc.  
494 Am. Bull., 85, 927-930, [https://doi.org/10.1130/0016-7606\(1974\)85<927:SOLAMV>2.0.CO;2](https://doi.org/10.1130/0016-7606(1974)85<927:SOLAMV>2.0.CO;2), 1974.
- 495 Franke, D.: Rifting, lithosphere breakup and volcanism: comparison of magma-poor and volcanic rifted margins,  
496 Marine and Petroleum Geology, 43, 63-87, <https://doi.org/10.1016/j.marpetgeo.2012.11.003>, 2013.
- 497 Franke, D., Savva, D., Pubellier, M., Steuer, S., Mouly, B., Auxietre, J., Meresse, F., and Chamot-Rooke, N.: The  
498 final rifting evolution in the South China Sea, Mar. Petrol. Geol., v. 58, p. 704-720,  
499 <https://doi.org/10.1016/j.marpetgeo.2013.11.020>, 2014.
- 500 Funck, T.: Structure of the volcanic apron north of Gran Canaria deduced from reflection seismic, bathymetric and  
501 borehole data, Ph.D. dissertation, University of Kiel, 156 pp., 1996.
- 502 Giordano, D., Russell, J.K., Dingwell, D.B.: Viscosity of magmatic liquids: a model, Earth Planet. Sci. Lett., 271,  
503 123-134, <https://doi.org/10.1016/j.epsl.2008.03.038>, 2008.
- 504 Goto, Y., and McPhie, J.: Morphology and propagation styles of Miocene submarine basanite lavas at Stanley,  
505 northwestern Tasmania, Australia, J. Volcanol. Geoth. Res., 130, 307-328, [https://doi.org/10.1016/S0377-0273\(03\)00311-1](https://doi.org/10.1016/S0377-0273(03)00311-1), 2004.



- 507 Grosse, P., and Kervyn, M.: Morphometry of terrestrial shield volcanoes, *Geomorphology*, 304, 1-14,  
508 <https://doi.org/10.1016/j.geomorph.2017.12.017>, 2018.
- 509 Greeley, R.: The role of lava tubes in Hawaiian volcanoes, U.S. Geological Survey Professional Paper 1350, 1589-  
510 1602, 1987.
- 511 Gregg, T.K.P., and Fornari, D.J.: Long submarine lava flows: Observations and results from numerical modeling, *J.*  
512 *Geophys. Res.*, v. 103, p. 27517-27531, <https://doi.org/10.1029/98JB02465>, 1998.
- 513 Griffiths, R.W. and Fink, J.H.: Solidification and morphology of submarine lavas: A dependence on extrusion rate,  
514 *J. Geophys. Res.*, 97(B13), 19729-19737, <https://doi.org/10.1029/92JB01594>, 1992.
- 515 Griffiths, R.W.: The Dynamics of lava flows, *Annu. Rev. Fluid Mech.*, 32, 477-518,  
516 <https://doi.org/10.1146/annurev.fluid.32.1.477>, 2000.
- 517 Hall, R.: Cenozoic geological and plate tectonic evolution of SE Asia and the SW Pacific: Computer-based  
518 reconstructions, model and animations, *J. Asian Earth Sci.*, 20, 353-431, [https://doi.org/10.1016/S1367-](https://doi.org/10.1016/S1367-9120(01)00069-4)  
519 [9120\(01\)00069-4](https://doi.org/10.1016/S1367-9120(01)00069-4), 2002.
- 520 He, Y.M., and Wen, L.X.: Seismic velocity structures and detailed features of the D'' discontinuity near the core-  
521 mantle boundary beneath eastern Eurasia, *Phys. Earth Planet. In.*, 189, 176-184,  
522 <https://doi.org/10.1016/j.pepi.2011.09.002>, 2011.
- 523 Holcomb, R.T., Moore, J.G., Lipman, P.W., and Belderson, R.H.: Voluminous submarine lava flows from Hawaiian  
524 volcanoes, *Geology*, 16, 400-404, [https://doi.org/10.1130/0091-7613\(1988\)016<0400:VSlava flow](https://doi.org/10.1130/0091-7613(1988)016<0400:VSlava flow fanH>2.3.CO;2)  
525 [fanH>2.3.CO;2](https://doi.org/10.1130/0091-7613(1988)016<0400:VSlava flow fanH>2.3.CO;2), 1988.
- 526 Ikegami, F., McPhie, J., Carey, R., Mundana, R., Soule, S.A. and Jutzeler, M.: The eruption of submarine rhyolite  
527 lavas and domes in the deep ocean–Havre 2012, Kermadec Arc, *Front. Earth Sci.*, 6, 147,  
528 <https://doi.org/10.3389/feart.2018.00147>, 2018.





- 529 Jackson, C.A.-L.: Seismic reflection imaging and controls on the preservation of ancient sill-fed magmatic vents, J.
- 530 Geol. Soc. London, 169, 503-506, <https://doi.org/10.1144/0016-76492011-147>, 2012.
- 531 Judd, A.G., and Hovland, M. (Eds.): Seabed Fluid Flow: The Impact on Geology, Biology and the Marine
- 532 Environment, Cambridge University Press, Cambridge, 2007.
- 533 Lester, R., Van Avendonk, H.J.A., McIntosh, K., Lavier, L., Liu, C.S., Wang, T.K., and Wu, F.: Rifting and
- 534 magmatism in the northeastern South China Sea from wide-angle tomography and seismic reflection imaging: J.
- 535 Geophys. Res., 119, 2305-2323, <https://doi.org/10.1002/2013JB010639>, 2014.
- 536 Li, C.F., Lin, J., Kulhanek, D.K., and the Expedition 349 Scientists: Proceedings of the International Ocean
- 537 Discovery Program, 349, <https://doi.org/10.14379/iodp.proc.349.103.2015>, 2015.
- 538 Li, C.F., Xu, X., Lin, J., Sun, Z., Zhu, J., Yao, Y.J., Zhao, X.X., Liu, Q.S., Kulhanek, D.K., Wang, J., Song, T.R.,
- 539 Zhao, J.F., Qiu, N., Guan, Y.X., Zhou, Z.Y., Williams, T., Bao, R., Briaies, A., Brown, E.A., Chen, Y.F., Clift, P.D.,
- 540 Colwell, F.S., Dadd, K.A., Ding, W.W., Almeida, I.H., Huang, X.L., Hyun, S., Jiang, T., Koppers, A.A.P., Li, Q.Y.,
- 541 Liu, C.L., Liu, Z.F., Nagai, R.H., Peleo-Alampay, A., Su, X., Tejada, M.L.G., Trin, H.S., Yeh, Y.C., Zhang, C.L.,
- 542 Zhang, F., and Zhang, G.L.: Ages and magnetic structures of the South China Sea constrained by the deep tow
- 543 magnetic surveys and IODP Expedition 349: Geochem. Geophys. Geosy., 15, 4958-4983,
- 544 <https://doi.org/10.1002/2014JB011686>, 2014.
- 545 Li, L., Clift, P.D., and Nguyen, H.T.: The sedimentary, magmatic and tectonic evolution of the southwestern South
- 546 China Sea revealed by seismic stratigraphic analysis, Mar. Geophys. Res., 34, 341-365,
- 547 <https://doi.org/10.1007/s11001-013-9171-y>, 2013.
- 548 Li, P., and Liang, H.: Cenozoic magmatism in the Pearl River Mouth Basin and its relationship to the basin evolution
- 549 and petroleum accumulation, Guangdong Geology, 9, 23-34, 1994.
- 550 Lüdmann, T., and Wong, H.K.: Neotectonic regime on the passive continental margin of the northern South China



- 551 Sea, Tectonophysics, 311, 113-138, [https://doi.org/10.1016/S0040-1951\(99\)00155-9](https://doi.org/10.1016/S0040-1951(99)00155-9), 1999.
- 552 Lüdmann, T., Wong, H.K., and Wang, P.: Plio-Quaternary sedimentation processes and neotectonics of the northern
- 553 continental margin of the South China Sea, Mar. Geol., 172, 331-356, <https://doi.org/10.1016/S0025->
- 554 3227(00)00129-8, 2001.
- 555 Magee, C., Hunt-Stewart, E., and Jackson, C.A.-L.: Volcano growth mechanisms and the role of sub-volcanic
- 556 intrusions: Insights from 2D seismic reflection data, Earth Planet. Sci. Lett., 373, 41-53,
- 557 <https://doi.org/10.1016/j.epsl.2013.04.041>, 2013.
- 558 Miles, A., and Cartwright, J.: Hybrid flow sills: A new mode of igneous sheet intrusion, Geology, 38, 343-346,
- 559 <https://doi.org/10.1130/G30414.1>, 2010.
- 560 Newman, S., and Lowenstern, J.B.: VolatileCalc: a silicate melt-H<sub>2</sub>O-CO<sub>2</sub> solution model written in Visual Basic for
- 561 excel, Comput. Geosci., 28, 597-604, [https://doi.org/10.1016/S0098-3004\(01\)00081-4](https://doi.org/10.1016/S0098-3004(01)00081-4), 2002,
- 562 Planke, S., Symonds, P., Alvestad, E., and Skogseid, J.: Seismic volcanostratigraphy of large-volume basaltic
- 563 extrusive complexes on rifted margins, J. Geophys. Res., 105, 19335-19351,
- 564 <https://doi.org/10.1029/1999JB900005>, 2000.
- 565 Qin, G.Q.: Application of micropaleontology to the sequence stratigraphic studies of late Cenozoic in the Pearl River
- 566 Mouth Basin, Marine Geology & Quaternary Geology, 16, 1-18, <https://doi.org/10.16562/j.cnki.0256->
- 567 1492.199.04.001, 1996.
- 568 Reynolds, P., Holford, S., Schofield, N., and Ross, A.: Three-dimensional seismic imaging of ancient submarine lava
- 569 flows: an example from the southern Australian margin, Geochem. Geophys. Geos., 18, 3840-3853,
- 570 <https://doi.org/10.1002/2017GC007178>, 2017.
- 571 Reynolds, P., Schofield, N., Brown, R.J. and Holford, S.P.: The architecture of submarine monogenetic volcanoes-
- 572 insights from 3D seismic data, Bas. Res., 30, 437-451, <https://doi.org/10.1111/bre.12230>, 2018.



- 573 Robinson, J.E., and Eakins, B.W.: Calculated volumes of individual shield volcanoes at the young end of the  
574 Hawaiian Ridge, *J. Volcanol. Geoth. Res.*, 151, 309-617, <https://doi.org/10.1016/j.jvolgeores.2005.07.033>, 2006.
- 575 Ru, K., and Pigott, J.D.: Episodic rifting and subsidence in the South China Sea, *AAPG Bull.*, 9, 1136-1155, 1986.
- 576 Shi, X., Kohn, B., Spencer, S., Guo, X., Li, Y., Yang, X., Shi, H., Gleadow, A.: Cenozoic denudation history of  
577 southern Hainan Island, South China Sea: constraints from low temperature thermochronology, *Tectonophysics*,  
578 504, 100-115, <https://doi.org/10.1016/j.tecto.2011.03.007>, 2011.
- 579 Sibuet, J.-C., Yeh, Y.-C., and Lee, C.-S.: Geodynamics of the South China Sea, *Tectonophysics*, 692, 98-119,  
580 <https://doi.org/10.1016/j.tecto.2016.02.022>, 2016.
- 581 Somoza, L., Gonzalez, F.J., Barker, S.J., Madureira, P., Medialdea, T., de Ignacio, C., Lourenco, N., Leon, R.,  
582 Vazquez, J.T., and Palomino, D.: Evolution of submarine eruptive activity during the 2011-2012 El Hierro event  
583 as documented by hydroacoustic images and remotely operated vehicle observations, *Geochem. Geophys. Geosy.*,  
584 18, 3109-3137, <https://doi.org/10.1002/2016GC006733>, 2017.
- 585 Sun, Q.L., Xie, X.N., Piper, D.J.W., Wu, J., and Wu, S.G.: Three dimensional seismic anatomy of multi-stage mass  
586 transport deposits in the Pearl River Mouth Basin, northern South China Sea: Their ages and kinematics, *Mar.*  
587 *Geol.*, 393, 93-108, <https://doi.org/10.1016/j.margeo.2017.05.005>, 2017.
- 588 Sun, Q.L., Wu, S.G., Cartwright, J., Wang, S.H., Lu, Y.T., Chen, D.X., and Dong, D.D.: Neogene igneous intrusions  
589 in the northern South China Sea: evidence from high resolution three dimensional seismic data, *Mar. Petrol. Geol.*,  
590 54, 83-95, <https://doi.org/10.1016/j.marpetgeo.2014.02.014>, 2014b.
- 591 Sun, Q.L., Wu, S.G., Cartwright, J., and Dong, D.D.: Shallow gas and focused fluid flow systems in the Pearl River  
592 Mouth Basin, northern South China Sea, *Mar. Geol.*, 315-318, 1-14, <https://doi.org/10.1016/j.margeo.2012.05.003>,  
593 2012.
- 594 Sun, Z., Xu, Z., Sun, L., Pang, X., Yan, C., Li, Y., Zhao, Z., Wang, Z., Zhang, C.: The mechanism of post-rift fault



- 595 activities in the Baiyun Sag, Pearl River Mouth Basin, J. Asian Earth Sci., 89, 76-87,  
596 <https://doi.org/10.1016/j.jseas.2014.02.018>, 2014a.
- 597 Taylor, B., and Hayes, D.E.: Origin and history of the South China Sea Basin, in: The Tectonic and Geologic  
598 Evolution of Southeast Asian Seas and Islands, edited by Hayes, D.E., AGU, Washington, DC, 23-56, 1983.
- 599 Thomson, K.: Determining magma flow in sills, dykes and laccoliths and their implications for sill emplacement  
600 mechanisms, B. Volcanol., 70, 183-201, <https://doi.org/10.1007/s00445-007-0131-8>, 2007.
- 601 Thomson, K., and Hutton, D.: Geometry and growth of sill complexes: Insights using 3-D seismic from the North  
602 Rockall Trough, B. Volcanol., 66, 364-375, <https://doi.org/10.1007/s00445-003-0320-z>, 2004.
- 603 Tu, K., Flower, M.F.J., Carlson, R.W., Zhang, M., Xie, G.: Sr, Nd, and Pb isotopic compositions of Hainan basalts  
604 (south China): implications for a subcontinental lithosphere Dupal source, Geology, 19, 567-569,  
605 [https://doi.org/10.1130/0091-7613\(1991\)019<0567:SNAPIC>2.3.CO;2](https://doi.org/10.1130/0091-7613(1991)019<0567:SNAPIC>2.3.CO;2), 1991.
- 606 Wang, T.K., Chen, M.K., Lee, C.S., and Xia, K.Y.: Seismic imaging of the transitional crust across the northeastern  
607 margin of the South China Sea, Tectonophysics, 412, 237-254, <https://doi.org/10.1016/j.tecto.2005.10.039>, 2006.
- 608 Wang, P., Prell, W.L., and ODP 184 scientists.: Proceedings of the Ocean Drilling Program, Initial Reports, 184.  
609 Ocean Drilling Program, College Station, TX 2000, 2000.
- 610 Walker, G.P.L.: Basaltic-volcano systems, in: Magmatic Processes and Plate Tectonics, edited by Pritchard, H.M.,  
611 Alabaster, T., Harris, N.B.W., and Neary, C.R., Geological Society Special Publication, 76, 3-38, 1993.
- 612 Wei, X.D., Ruan, A.G., Zhao, M.H., Qiu, X.L., Li, J.B., Zhu, J.J., Wu, Z.L., and Ding, W.W.: A wide-angle OBS  
613 profile across the Dongsha uplift and Chaoshan depression in the mid-northern South China Sea, Chinese J.  
614 Geophys-CH., 54, 3325-3335, <https://doi.org/10.3969/j.issn.0001-5733.2011.12.030>, 2011.
- 615 Wu, S.G., Gao, J.W., Zhao, S.J., Lüdmann, T., Chen, D.X., and Spence, G.: Post-rift uplift and focused fluid flow in  
616 the passive margin of Northern South China Sea, Tectonophysics, 615-616, 27-39,



- 617 <https://doi.org/10.1016/j.tecto.2013.12.013>, 2014.
- 618 Xia, S.H., Zhao, D.P., Sun, J.L., and Huang, H.B.: Teleseismic imaging of the mantle beneath southernmost China:  
619 new insights into the Hainan plume, *Gondwana Res.*, 36, 33-43, <https://doi.org/10.1016/j.gr.2016.05.003>, 2016.
- 620 Xie, Z.Y., Sun, L.T., Pang, X., Zheng, J.Y., and Sun, Z.: Origin of the Dongsha Event in the South China Sea: *Mar.*  
621 *Geophys. Res.*, 38, 357-371, <https://doi.org/10.1007/s11001-017-9321-8>, 2017.
- 622 Xu, S.C., Yang, S.K., and Huang, L.F.: The application of sequence stratigraphy to stratigraphic correlation, *Earth*  
623 *Sci. Front.*, 2, 115-123, 1995.
- 624 Yan, P., Deng, H., Liu, H.L., Zhang, Z., and Jiang, Y.: The temporal and spatial distribution of volcanism in the South  
625 China Sea region, *J. Asian Earth Sci.*, 27, 647-659, <https://doi.org/10.1016/j.jseaes.2005.06.005>, 2006.
- 626 Yan, P., Wang, Y.L., Liu, J., Zhong, G.J., and Liu, X.J.: Discovery of the southwest Dongsha Island mud volcanoes  
627 amid the northern margin of the South China Sea, *Mar. Petrol. Geol.*, 88, 858-870,  
628 <https://doi.org/10.1016/j.marpetgeo.2017.09.021>, 2017.
- 629 Yan, P., Zhou, D., and Liu, Z.S.: A crustal structure profile across the northern continental margin of the South China  
630 Sea, *Tectonophysics*, 338, 1-21, [https://doi.org/10.1016/S0040-1951\(01\)00062-2](https://doi.org/10.1016/S0040-1951(01)00062-2), 2001.
- 631 Yang, S., Qiu, Y., and Zhu, B.: Atlas of Geology and Geophysics of the South China Sea, China Navigation  
632 Publications, Tianjin, 2015.
- 633 Yu, H.S.: Structure, stratigraphy and basin subsidence of Tertiary basins along the Chinese southeastern continental  
634 margin, *Tectonophysics*, 253, 63-76, 1994.
- 635 Zhang, N., and Li, Z.X.: Formation of mantle “lone plumes” in the global downwelling zone - A multiscale modelling  
636 of subduction-controlled plume generation beneath the South China Sea, *Tectonophysics*, 723, 1-13,  
637 <https://doi.org/10.1016/j.tecto.2017.11.038>, 2018.
- 638 Zhao, F., Alves, T.M., Wu, S.G., Li, W., Huuse, M., Mi, L.J., Sun, Q.L., and Ma, B.J.: Prolonged post-rift magmatism



639 on highly extended crust of divergent continental margins (Baiyun Sag, South China Sea), Earth Planet. Sci. Lett.,  
640 445, 79-91, <https://doi.org/10.1016/j.epsl.2016.04.001>, 2016.

641 Zhao, F., Wu, S.G., Sun, Q.L., Huuse, M., Li, W., and Wang, Z.J.: Submarine volcanic mounds in the Pearl River  
642 Mouth Basin, northern South China Sea, Mar. Geol., 355, 162-172, <https://doi.org/10.1016/j.margeo.2014.05.018>,  
643 2014.

644 Zhao, S.J., Wu, S.G., Shi, H.S., Dong, D.D., Chen, D.X., and Wang, Y.: Structures and dynamic mechanism related  
645 to the Dongsha Event at the northern margin of the South China Sea, Progress in Geophysics, 27, 1008-1019,  
646 <https://doi.org/10.6038/j.issn.1004-2903.2012.03.022>, 2012.

647 Zou, H., Li, P., and Rao, C.: Geochemistry of Cenozoic volcanic rocks in Zhu Jiangkou Basin and its geodynamic  
648 significance, Geochimica, 24, 33-45, 1995.

649

650



## 651 Tables

652

653 Table 1: Dimensions of volcano edifices. <sup>a</sup>diameter and dip are average values.

Volcano edifice	<sup>a</sup> Diameter/m	Height/m	Area/km <sup>2</sup>	Volume/km <sup>3</sup>	<sup>a</sup> Dip/°
Volcano edifice 1 (V1)	3018	404±101	7.15	0.940±0.235	15.0±3.6
Volcano edifice 1 (V2)	714	200±50	0.44	0.030±0.008	27.8±5.9

654

655 Table 2: Dimensions of lava flow apron. <sup>a</sup>Diameter is calculated from the area as a circle. V =

656 Volcano edifice.

Lava flow apron	Diameter (m)	Area (km <sup>2</sup> )	Thickness (m)	Volume (km <sup>3</sup> )	Feeder	Shape
Lava flow apron	3182 <sup>a</sup>	7.95	80±20	0.637±0.159	V1	Ring

657

658 Table 3: Dimensions of lava flow channels (C). Please note that all the lengths of lava flow

659 channels are measured along their axes. <sup>a</sup>Maximum lengths (including the inferred part of lava

660 flow channels); <sup>b</sup>Minimum length (C3 extends beyond the 3D survey); <sup>c</sup>Thickneses cannot be

661 measured, because of lava flow channels (C1 and C2) are only identified on the plan-view map

662 (RMS and variance slice map); <sup>d</sup>Area and volume don't include the inferred part of C5.

Lava flow channels		Length (km)	Width (m)	Thickness (m)	Area (km <sup>2</sup> )	Volume (km <sup>3</sup> )
Volcano edifices 1-related	C1	2.86 <sup>a</sup>	55-273	unknown <sup>c</sup>	0.31 <sup>a</sup>	unknown <sup>c</sup>
	C2	3.66 <sup>a</sup>	94-340	unknown <sup>c</sup>	0.56 <sup>a</sup>	unknown <sup>c</sup>
	C3	4.60 <sup>b</sup>	163-340	52±13	0.84 <sup>a</sup>	0.044±0.011
Volcano edifices 2-related	C4	2.80	172-229	61±15	0.54	0.032±0.008
	C5	9.15 <sup>a</sup>	185-267	64±16	1.52 <sup>d</sup>	0.097±0.024 <sup>d</sup>
	C6	6.39	203-285	60±15	1.47	0.088±0.022
	C7	1.93	236-427	57±14	0.67	0.037±0.009

663

664 Table 4: Dimensions of lava flow fans. <sup>a</sup>Diameter is calculated from the area as a circle.



<sup>b</sup>Minimum areas and volumes, because of limited data coverage. C = Lava flow channel; S = Sill.

Lava flow fans	Diameter (m)	Area (km <sup>2</sup> )	Thickness (m)	Volume (km <sup>3</sup> )	Feeder	Shape
Lava flow fan 1 (F1)	944 <sup>a</sup>	0.70	41±10	0.028±0.007	C1	Lobate
Lava flow fan 2 (F2)	1050 <sup>a</sup>	0.87	41±10	0.035±0.009	C1	Lobate
Lava flow fan 3 (F3)	997 <sup>a</sup>	0.78 <sup>b</sup>	41±10	0.031±0.008 <sup>b</sup>	C1	Lobate
Lava flow fan 4 (F4)	2171 <sup>a</sup>	3.70 <sup>b</sup>	41±10	0.148±0.037 <sup>b</sup>	C2	Lobate
Lava flow fan 5 (F5)	3054 <sup>a</sup>	7.32	109±27	0.791±0.198	C5/C6	Lobate
Lava flow fan 6 (F6)	7906 <sup>a</sup>	49.07 <sup>b</sup>	55±14	2.650±0.662 <sup>b</sup>	S1/S2	Lobate





## Figures

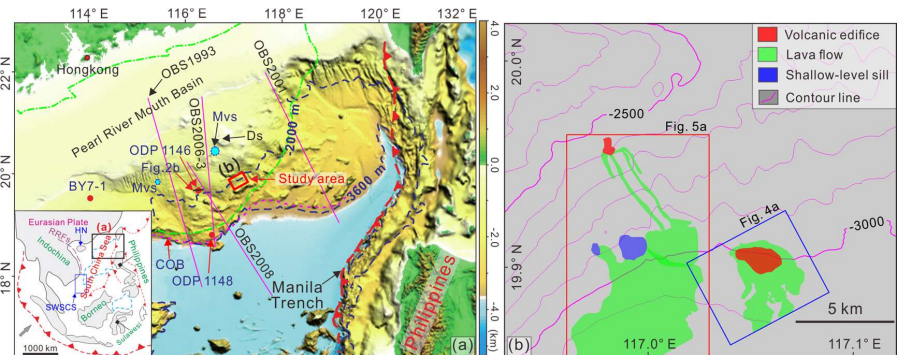


Figure 1: Geological setting of the study area. (a) Bottom-left: regional setting of the South China Sea that is bounded by the Red River Strike-slip faults (RRFs) to the west and by the subduction trench (Manila Trench) to the east. Hainan Island (HN; Tu et al., 1991; Shi et al., 2011) and southwestern South China Sea (SWSCS; Li et al., 2013) in which the magmatism has the similar ages with the studied volcanoes are labelled. The study area (marked with red square) is located to the south of Dongsha Islands. The green dashed line outlines the boundary of Pearl River Mouth Basin. Locations of boreholes (Exploration well BY7-1 and ODP sites 1146 and 1148), crustal structure profiles (OBS1993 (Yan et al., 2001), OBS2001 (Wang et al., 2006), OBS2006-3 (Wei et al., 2011), and OBS2008 (Chiu, 2010)) and mud volcanoes (Mvs; Sun et al., 2012; Yan et al., 2017) are labeled. Ds = Dongsha Islands; COB = Continent ocean boundary (Adopted from Sibuet et al., 2016). The base map is modified from Yang et al. (2015). (b) Seabed morphologies of the study area. Distributions of volcano edifices (red), sills (blue), lava flows (green) and locations of Figures 4a and 5a are labeled. The contour lines are in 100 ms (two).





685

686

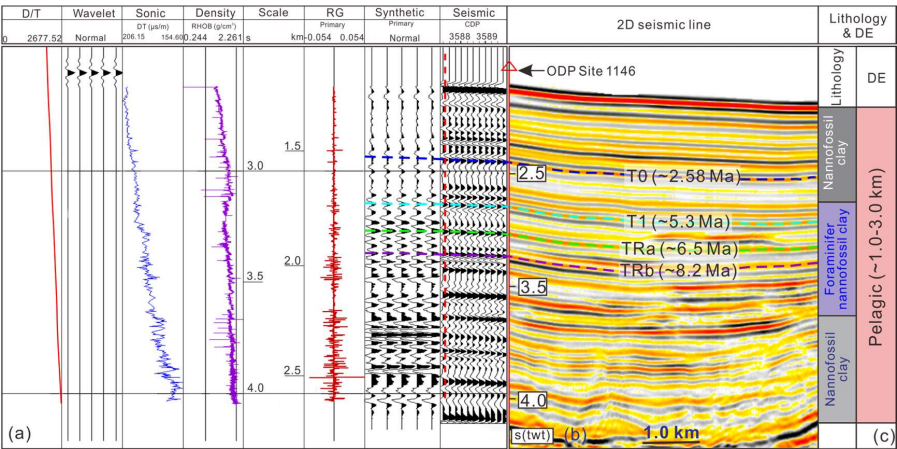
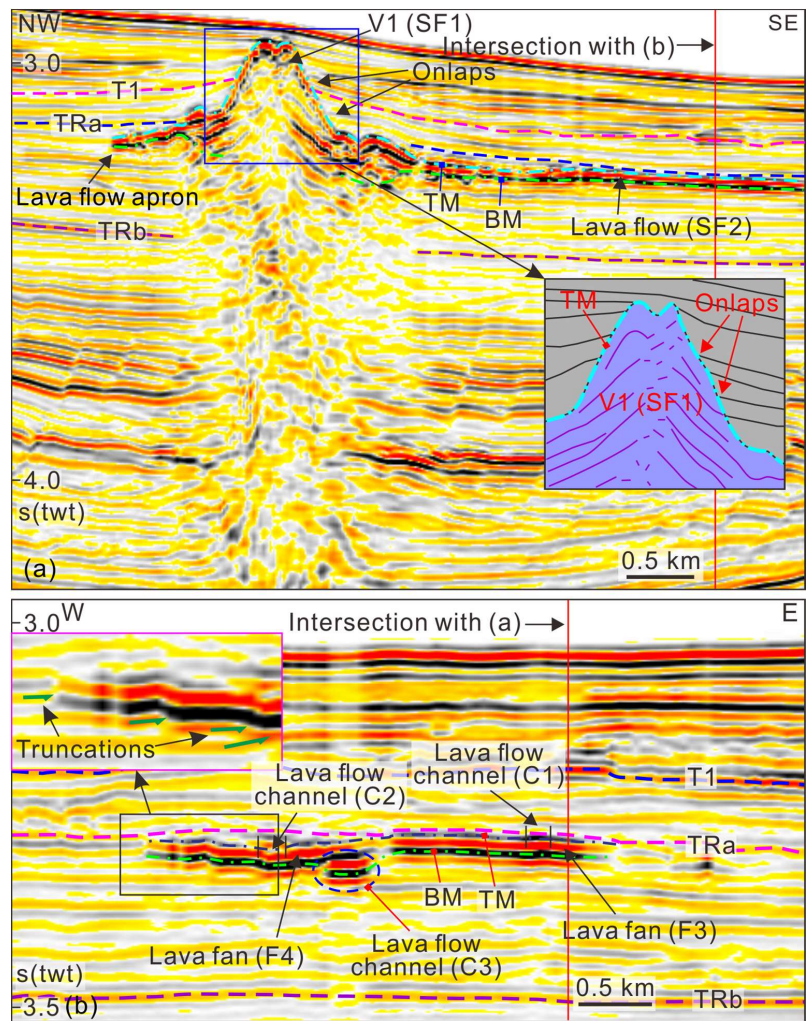


Figure 2: (a) Synthetic seismogram of ODP Site 1146 (Modified from Sun et al., 2017); (b) Seismic profile crossing through ODP Site 1146. The four seismic surfaces (T0 (~2.58 Ma), T1 (~5.3 Ma), TRa (~6.5 Ma) and TRb (~8.2 Ma)) are labeled. D/T=Depth/time; DT=interval transit time; RHOB = lithologic density; RC = reflection coefficient; (c) Lithology and depositional environment (DE) of ODP Site 1146 (Modified from Wang et al. (2000) and Clift et al. (2001)).

692



693



694

695 Figure 3: Seismic characteristics of deep-water volcano (V1) and associated lava flow channels/fans.

696 (a) Seismic profile crosscuts the volcano edifice and associated lava flow; (b) Seismic profile

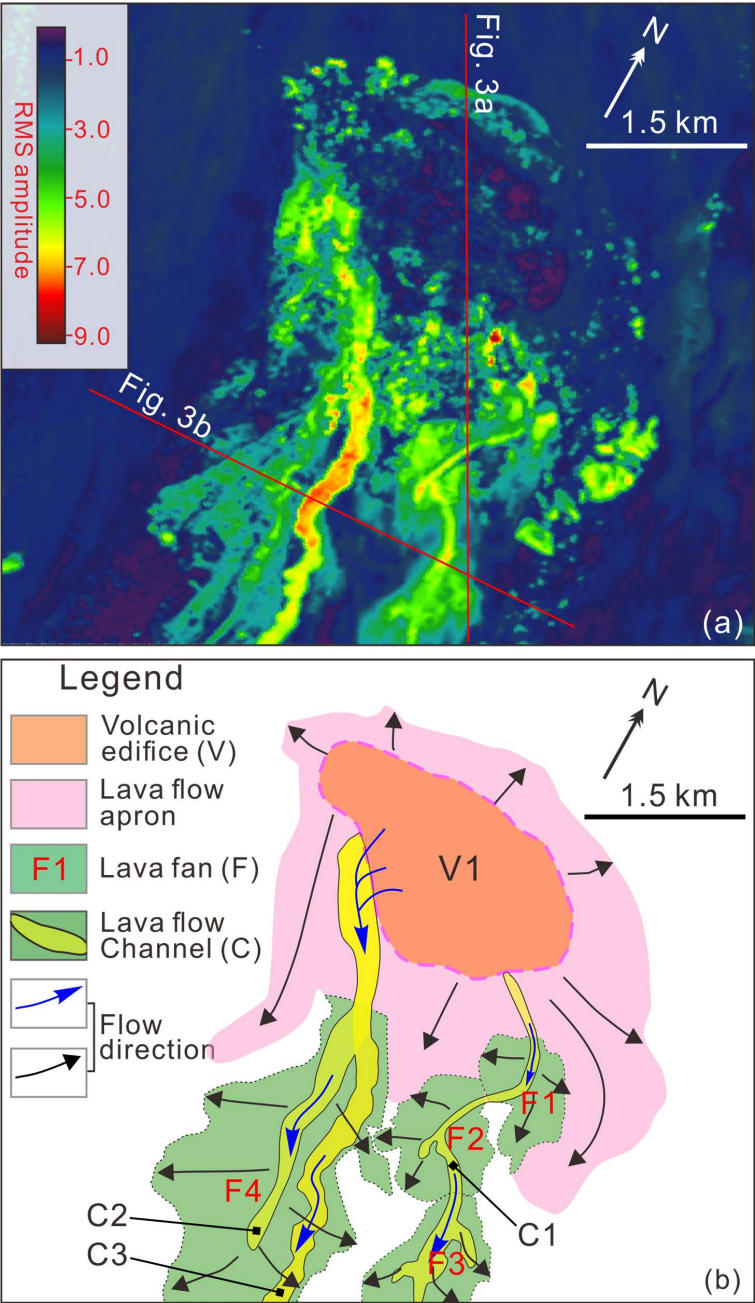
697 crosscuts the lava flow (enhanced seismic anomalies). TM = top of volcano/lava flow; BM = base

698 of volcano/lava flow. See locations in Figure 4.

699



700



701

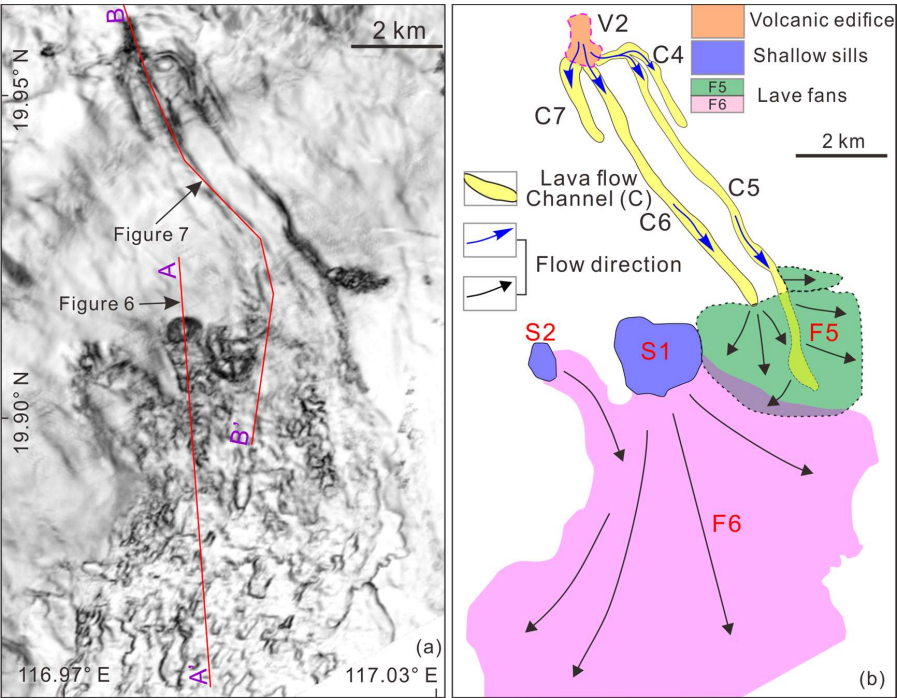
702 Figure 4: (a) and (b) RMS amplitude map ( $\pm 30$  ms along the surface BM) and its interpretations.

703 Volcanic apron, lava flow channels/fans are labeled. See location in Figure 1b.





704



705

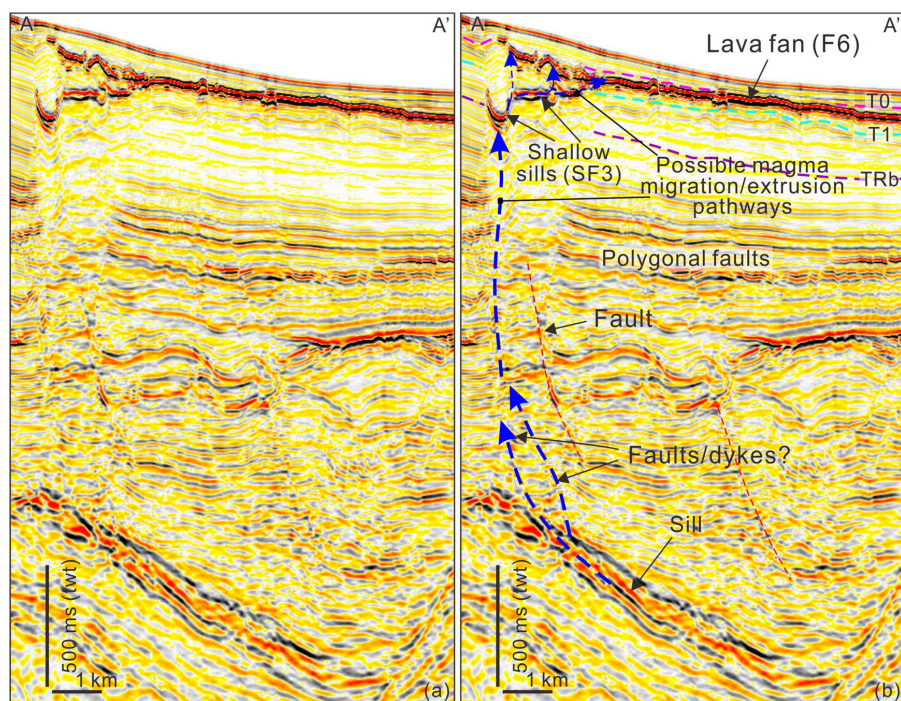
706 Figure 5: (a) and (b) Variance slice (extracted from the surface BM) and its interpretations. Lava

707 flows are clearly identified and marked. C = lava flow channel; S = shallow sill; F = lava fan.

708



709



710

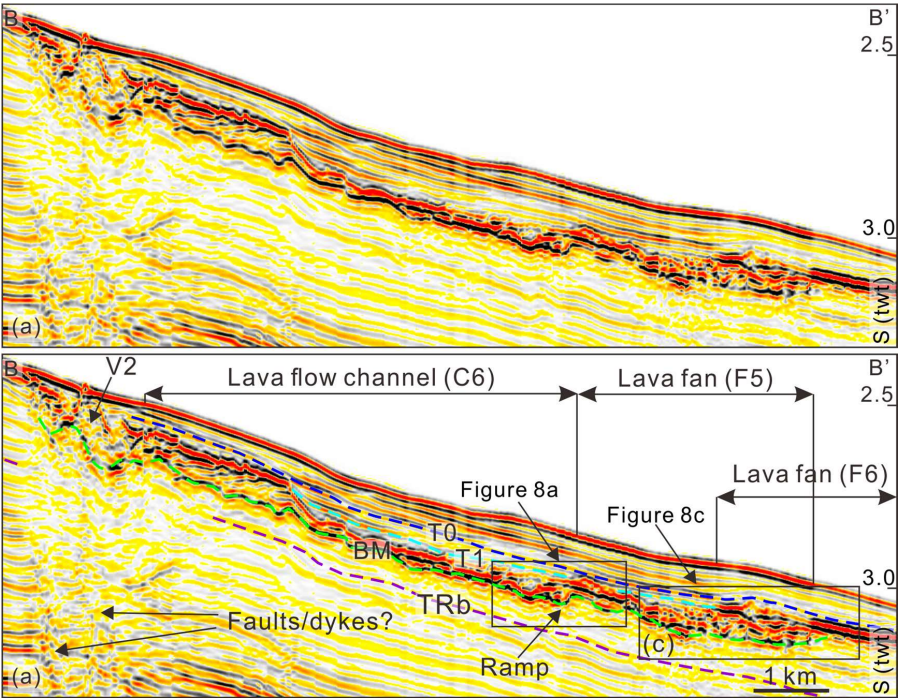
711 Figure 6: Seismic profile (a) and its interpretation show magma plumbing system from deep-seated

712 sill, shallow sill (S1) and lava fan (F6). See location in Figure 5a.

713



714

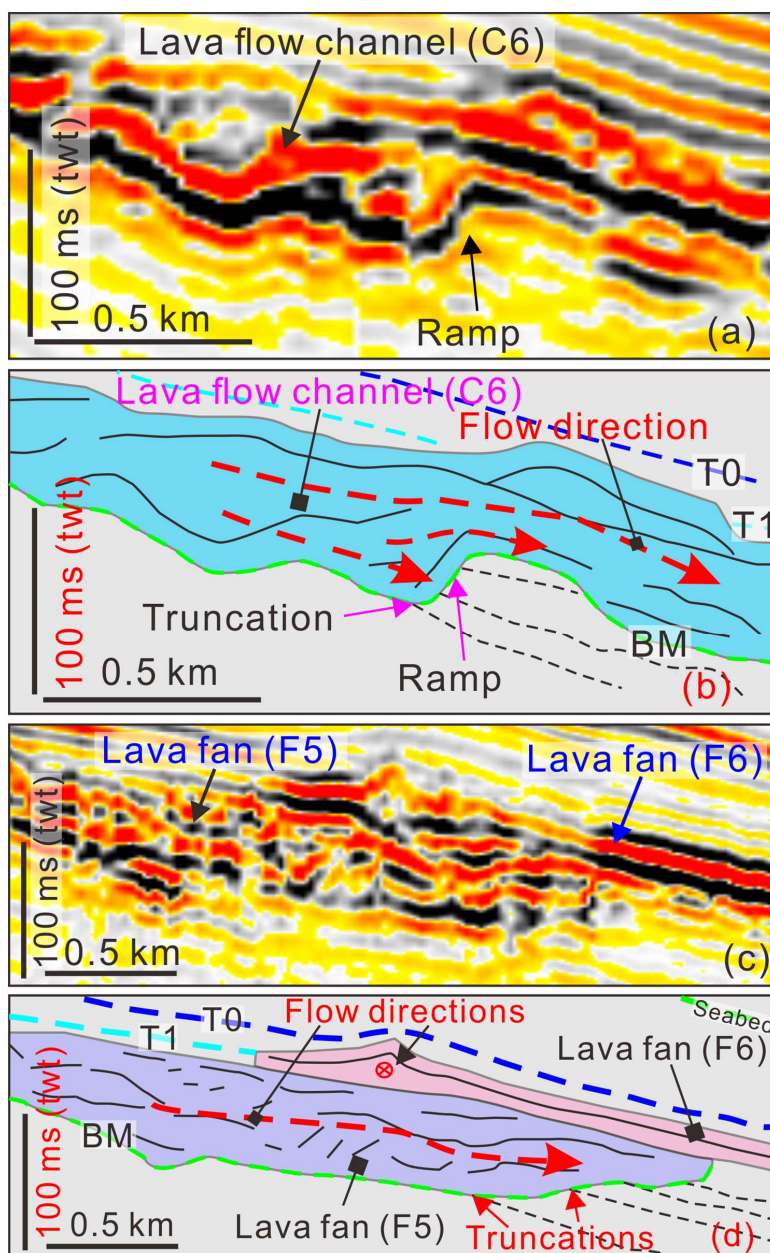


715

716 Figure 7: (a) Seismic profile crosscuts V2 and along lava flow channel (C6) and Lava fans (F5 and  
717 F6). The V2 has a sharp boundary to the upslope. Lava fan 6 (F6) is directly overlying the Lava fan  
718 5 (F5). BM = base of volcano/lava flow; See location in Figure 5a.

719





720

721 Figure 8: (a) and (b) Enlargement of the end of lava flow channel (ramp structure) and its line

722 drawings; (c) and (d) Enlargement and its line drawings of the lava fans (F5 and F6). BM = base of

723 volcano/lava flow. See locations in Figure 7.